JGR Space Physics

Key Points:

- Plasma irregularities over Troll and SANAE-4 stations in Queen Maud Land, Antarctica are associated with the edges of expanding auroral oval
- Plasma irregularities are related to strong plasma flow shears modulated by auroral particle precipitations
- Ionospheric structuring is reflected in enhanced phase scintillation index

Correspondence to:

D. S. Kotova,
daria.kotova@fys.uio.no

Case Studies of Ionospheric Plasma Irregularities Over Queen Maud Land, Antarctica

Arnlaug H. Skjæveland[1,2], Daria S. Kotova[1] (ID)**, and Wojciech J. Miloch[1]** (ID)

[1]Department of Physics, University of Oslo, Oslo, Norway, [2]Norwegian Mapping Authority, Oslo, Norway

Abstract We use the first data set from the ground-based TEC and scintillation receiver located at the Norwegian Research Station Troll in Queen Maud Land, Antarctica to analyze in detail the ionospheric response during geomagnetic disturbances on February 26–27 and March 18–19, 2018. By combining the Troll data with complementary measurements (scintillation receivers, magnetometers, SuperDARN, DMSP satellites), we demonstrate that plasma irregularities above this part of Queen Maud Land can be associated with the expansion of the auroral oval, related structuring on its edges, as well as with strong flow shears in the evening and at nighttime, which are further modulated by the energetic particle precipitation. Phase scintillation indices correlate well with the magnetometer data.

1. Introduction

The variability of ionospheric plasma in the polar regions is strongly related to complex coupling between the ionosphere and magnetosphere (Kamide & Baumjohann, 1993). Physical processes in the ionosphere such as plasma instabilities and turbulence can result in plasma structuring and irregularities at various scales. Such irregularities can in turn impact the propagation of trans-ionospheric radio waves through diffractive and refractive processes, and consequently lead to scintillations in the phase and amplitude of the received wave. Hence, the quality of services relying on radio signals, such as the Global Navigation Satellite Systems (GNSS) can be reduced. On the other hand, while monitoring such signals, one can infer the state of the ionosphere, and with supporting data, associate the plasma irregularities with physical processes in the ionosphere.

A common approach to ionospheric scintillations is the phase screen model, which assumes a thin layer of irregularities that acts as a phase screen, where the wave propagation is disturbed by the Huygens principle. As the wave propagates further, scintillations can occur both in phase and amplitude (Yeh & Liu, 1982). For spatial scales of irregularities less than the radius of the first-Fresnel zone ($r_F = \sqrt{\lambda L}$, where λ–is the wavelength of the signal and L–is the distance between the receiver and irregularity layer), both phase and amplitude scintillations are present. For the GNSS signals in the L-band, the Fresnel scale at 350 km altitude is ca. 360 m, but note that the effective Fresnel frequency is drift dependent (Forte & Radicella, 2002; Ghobadi et al., 2020; Wang et al., 2018).

At high latitudes (i.e., in the polar regions), observations of disturbances in the phase of received signal prevail over those in the amplitude of the signal. Phase scintillations are often observed near the ionospheric trough and in the vicinity of the boundary of the auroral oval, in particular around the magnetic midnight (Spogli et al., 2009). They are also observed in the polar cap at the edges of strong density gradients (and the corresponding gradients in the Total Electron Content, TEC) (Mitchell et al., 2005; Moen et al., 2013). Amplitude and phase scintillation often maximize close to TEC gradients at the edges of plasma patches, revealing the presence of small-scale irregularities, and can also be associated with a tongue of ionization (De Franceschi et al., 2008). In a climatological study, Prikryl et al. (2015) find the largest occurrence of scintillations in the Northern Hemisphere (NH) in the polar cap and in the night side of the auroral oval. They also note that with increasing solar and geomagnetic activities, the phase scintillations are more frequent and are present both poleward and equatorward from the statistical auroral oval.

We note, that the phase scintillation index σ_ϕ, being the standard deviation of the measured phase of the received signal and which is commonly used for characterizing phase scintillations, is sensitive to the drift velocity of plasma and thus to the detrending frequencies. Hence, a standard use of such indices might also include refractive variations when the plasma flow is large (Beach, 2006; Wang et al., 2018), leading

to seemingly larger occurrence of phase scintillations as compared to amplitude scintillations. Thus, the phase scintillation index, σ_ϕ, can be used as an indication of the variability and structuring of plasma density, and it should be analyzed with other supporting observations, as it does not necessarily relate to the actual diffractive scintillations of the GNSS signals (McCaffrey & Jayachandran, 2019). In our work, we use the phase scintillations index as a measure of variations in the plasma density rather than in the context of scintillations due to diffractive effects.

Most studies on ionospheric response to geomagnetic activity have focused on the NH. This is due to a much larger number of ground-based instruments in the NH compared to the Southern Hemisphere (SH), which facilitate for example scintillation studies (e.g., Jin et al., 2015; Moen et al., 2013; Prikryl et al., 2010, 2011, 2015; Spogli et al., 2009). However, the ionospheric response can be different in the SH and NH, in particular at high latitudes (Prikryl et al., 2011; Workayehu et al., 2019). The differences are usually attributed to the structure of the ionosphere, seasonal variations in the ionosphere and the solar zenith angle, or orientation of the interplanetary magnetic field (IMF) and related ionospheric convection patterns in the polar regions. Very often, the interhemispheric asymmetries are attributed to the magnetic anomaly in the SH and a significantly larger shift in the location of the geomagnetic pole from the geographical pole in the SH as compared to the NH (Laundal et al., 2017). As the instrument network in Antarctica is still very sparse, there are much fewer climatological studies in the high-latitude SH (Alfonsi et al., 2011; Cilliers et al., 2017; Deshpande et al., 2012; Kim et al., 2014; Kinrade et al., 2012; G. Li et al., 2010; Ngwira et al., 2010; Priyadarshi et al., 2018).

In December 2017, the University of Oslo established an ionospheric observatory at the Norwegian Research Station Troll in Queen Maud Land, Antarctica, which is located on the equatorward side of the quiet auroral oval, and in a relative proximity to the South Atlantic Magnetic Anomaly and the Weddel Sea Anomaly (Chen et al., 2019; Horvath & Lovell, 2009; Karpachev et al., 2011). Thus, the observatory is in the optimal location to study the ionospheric response to geomagnetic disturbances, and it fills the observational gap in this region of Antarctica. It is also a permanent research station that is located furthest south in Queen Maud Land.

In this study, we use the first data set from the GNSS TEC and scintillation receiver at Troll Ionospheric Observatory to study the ionospheric response to geomagnetic events on February 26–27 and March 18–19, 2018. The data from Troll are complemented with relevant datasets from neighboring stations in Queen Maud Land (SANAE-IV and Neumayer), radars, and satellites. Thus, this paper also demonstrates how combining different datasets can give insight into processes leading to observed plasma irregularities. While a similar multi-instrumental study was presented in past by Prikryl et al. (2011), where the authors focused on a different part of Antarctica, in our work we examine in more detail the sources of plasma irregularities observed above Troll and SANAE-IV, as well as dynamics of the irregularities.

2. Instruments

Two types of GNSS Ionospheric Scintillation and TEC Monitor (GISTM) receivers were used in this study: NovAtel GSV4004B and NovAtel GPStation-6. The GPStation-6 receiver was installed at the Norwegian Research Station Troll in December 2017. The receiver records signals from the GPS, GLONASS, and Galileo satellites, and it outputs raw observational data every second, including 50 Hz phase and amplitude measurements and 1 Hz TEC measurements. In addition, it can provide extended summary messages, including satellite azimuth/elevation angles, lock time, estimates of the amplitude ($S4$) and phase (σ_ϕ) scintillation indices, and TEC. Scintillation index $S4$ is defined as the normalized variance of the signal intensity (Yeh & Liu, 1982), while σ_ϕ is the standard deviation of the measured phase (e.g., more in Rino, 1979). The raw phase measurements are first detrended with a 6th-order Butterworth high-pass filter with a 0.1 Hz cutoff frequency, and the one-minute statistics of residuals are computed over periods of 1, 3, 10, 30, and 60 s. In this study, phase parameters for lock time less than 240 s were discarded, and we only use 60-second measurements for σ_ϕ. The lock time indicates how long the receiver has been locked to the carrier phase on the signal. To avoid some multipath effects identified at certain azimuth angles at the antenna location, we use the cut-off elevation angle of 30°.

Table 1
Details of the Ground-Stations Included in This Study

Station code	Station name	Geographic coordinates	Magnetic coordinates	MLT Feb/Mar	Instrument
VNA	Neumayer	70.7ºS 8.3ºW	60.6ºS 42.5ºE	21.6/21.8	Magnetometer
SNA	SANAE-IV	71.7ºS 2.8ºW	62.0ºS 42.1ºE	21.8/22.0	Magnetometer / GISTM / SuperDARN
TRL	Troll	72.0ºS 2.5ºE	62.8ºS 47.8ºE	22.0/22.2	GISTM

Note. The magnetic local time (MLT) is given with respect to midnight UT on February 26 and March 18, 2018.

To complement the Troll data set, we use data from the GSV4004B receiver at the SANAE-IV research station (located 186 km NW from Troll, Figure S1 shows the map with selected stations). The receiver is operated by the South African National Space Agency (SANSA). The noise levels of receivers at both stations have been plotted and compared. While for Troll, the median phase scintillation, which can be associated with noise, was 0.11 radians, for the receiver at SANAE-IV it was 0.05 radians. To eliminate multipath effects at SANAE-IV we used the same threshold as at Troll, i.e., the elevation angle of 30°. When analyzing data from both receivers, we used the thin ionospheric layer approach with the ionospheric piercing point (IPP) at 350 km (M. Li et al., 2018). The magnetic coordinates are calculated using the altitude adjusted corrected geomagnetic (AACGM) coordinates (Shepherd, 2014).

Complementary datasets include the magnetometer data from SANAE-IV and Neumayer research stations, geomagnetic indices and solar wind data from NASA's OMNIWeb Service, data from Defense Meteorological Satellite Program (DMSP) satellites, and from the Super Dual Auroral Radar Network (SuperDARN). The OMNI solar wind data are obtained with the ACE and Dscovr satellites and are time-shifted to the Earth's magnetopause. DMSP satellites carry, among other instruments, the Special Sensor Ionospheric Plasma Drift/Scintillation Monitor (SSI/ES-3) consisting of a Langmuir probe and ion sensor, and providing information on ion and electron densities, temperatures and average ion molecular weight (https://earth.esa.int/web/eoportal/satellite-missions/d/dmsp-block-5d). In addition, DMSP Special Sensor Ultraviolet Spectrographic Imager (SSUSI) measures UV radiation corresponding to auroral emissions and provides images of auroral intensity (Knight et al., 2008). SuperDARN is a network of high-frequency radars distributed over NH and SH, and it can be used for reconstructing the ionospheric convection at high latitudes. SuperDARN measurements rely on the Bragg backscatter from ionospheric plasma irregularities and the Doppler shift of the returning signal to determine the line-of-sight velocity of ionospheric plasma (Greenwald et al., 1995). Thus, these data also provide information about the amount of irregularities in the ionosphere and their velocities.

The ground-based instruments used in this study are located at stations in Queen Maud Land, Antarctica. The stations' geographical and magnetic coordinates, magnetic local time (MLT) during the selected geomagnetic events, and relevant instruments used in this study are given in Table 1.

3. Geomagnetic Conditions

Geomagnetic events were selected for the analysis based on the availability of data from all relevant instruments in year 2018 for active geomagnetic conditions, with the planetary index $Kp > 4$. Two time periods were identified: Case A: February 26–27th with $Kp = 5$ and with the longitudinally symmetric disturbance index $SYM\text{-}H = -34$ nT, and Case B: March 18–19th with $Kp = 6$ and $SYM\text{-}H = -53$ nT.

3.1. Conditions for Case A: February 26–27th, 2018

Figure 1 shows the IMF conditions, as well AE, and $SYM\text{-}H$ indices for the first event on February 26–27th. From 22:00 UT to 02:00 UT, the IMF B increases up to 10 nT, and it stays high until the end of the event (Figure 1a). This value is twice the typical magnitude of the IMF, which is considered to be 5 nT (as indicated in Prölss, 2004). Thus, strong field variations are observed, which are typical during geomagnetic disturbances. Variations in the IMF B_y component (Figure 1b) become more significant after 22 UT. IMF B_y is mostly negative except for time intervals between 18:00-19:30 UT, 23:00-00:30 UT, and 03:00-04:00 UT. Thus, we can
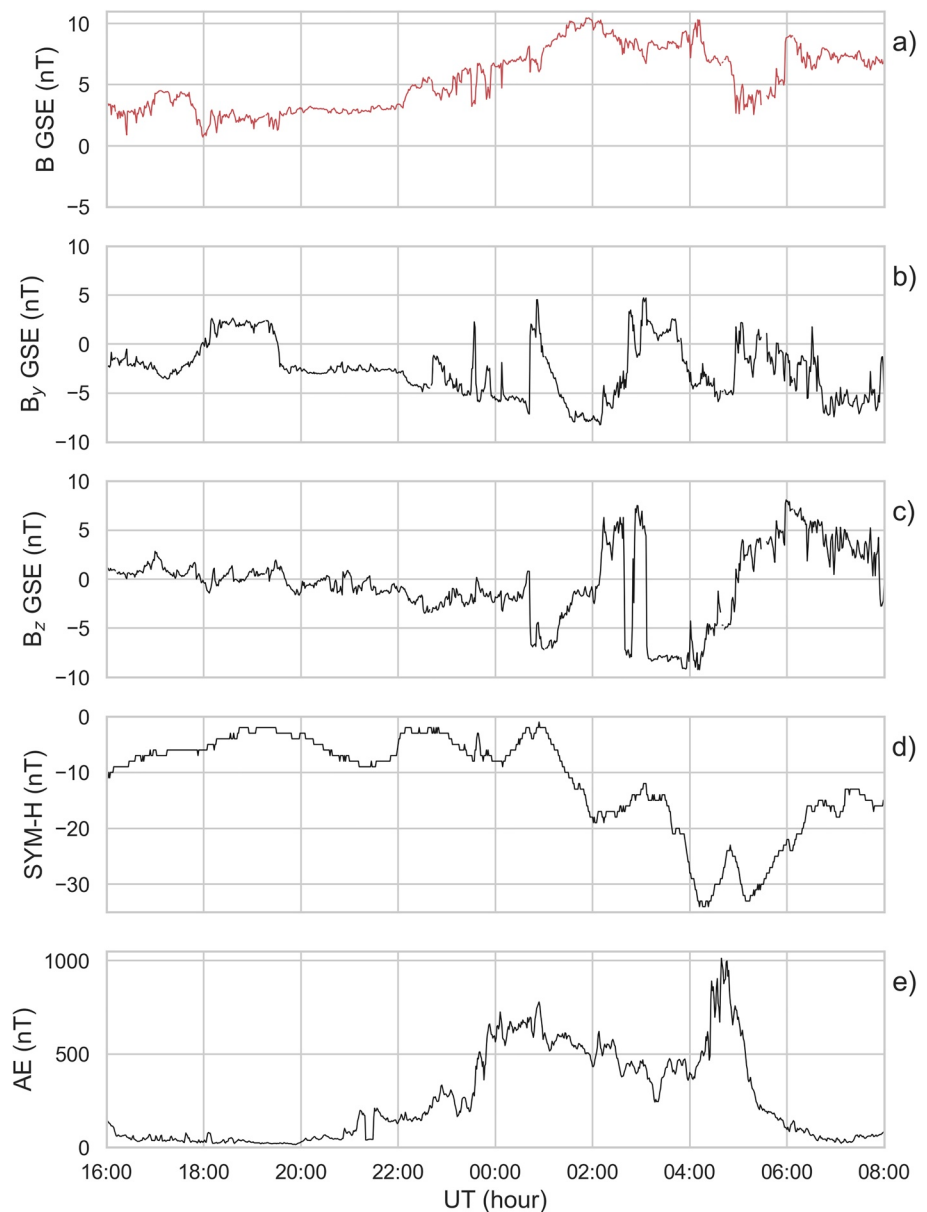
Figure 1. The interplanetary magnetic field (IMF) data time-shifted to the position of the bow shock, and the *AE* and *SYM-H* indices as a function of time, between 16:00 UT February 26th–08:00 UT February 27th: (a) the IMF *B* total magnitude, (b) IMF B_y component, (c) IMF B_z component, (d) *SYM-H* index, and (e) *AE* index.

expect that during these times, the polar cap potential in the SH is higher and that the convection cells are asymmetric (Clauer et al., 1984; Förster & Haaland, 2015; Heelis, 1984; Reiff & Burch,, 1985). The IMF B_z component (Figure 1c) gets weakly negative after 21:30 UT. Before 01 UT a sharp drop to −7 nT is observed, which is followed by a gradual change toward positive values. Another period of negative *Bz*, lasting for more than one hour, starts at around 03 UT. The IMF is variable after 22:00 UT facilitating reconnection on the dayside, hence the relatively cold and dense solar wind plasma (not shown in the figure) can enter the Earth's magnetosphere and lead to enhanced ionospheric convection.

Prolonged periods of negative B_z can give rise to reconnection in the magnetotail and hence geomagnetic substorms, as it is also suggested by the *AE* index shown in Figure 1e. Before 20:00 UT the *AE* index is at ca. 20 nT indicating quiet conditions, but between 20:00 and 00:00 UT it reaches 600 nT. At 01:00 UT, it starts to decrease slowly, with another peak (1,000 nT) at 04:40 UT. Afterward, the *AE* index decreases to 30nT at
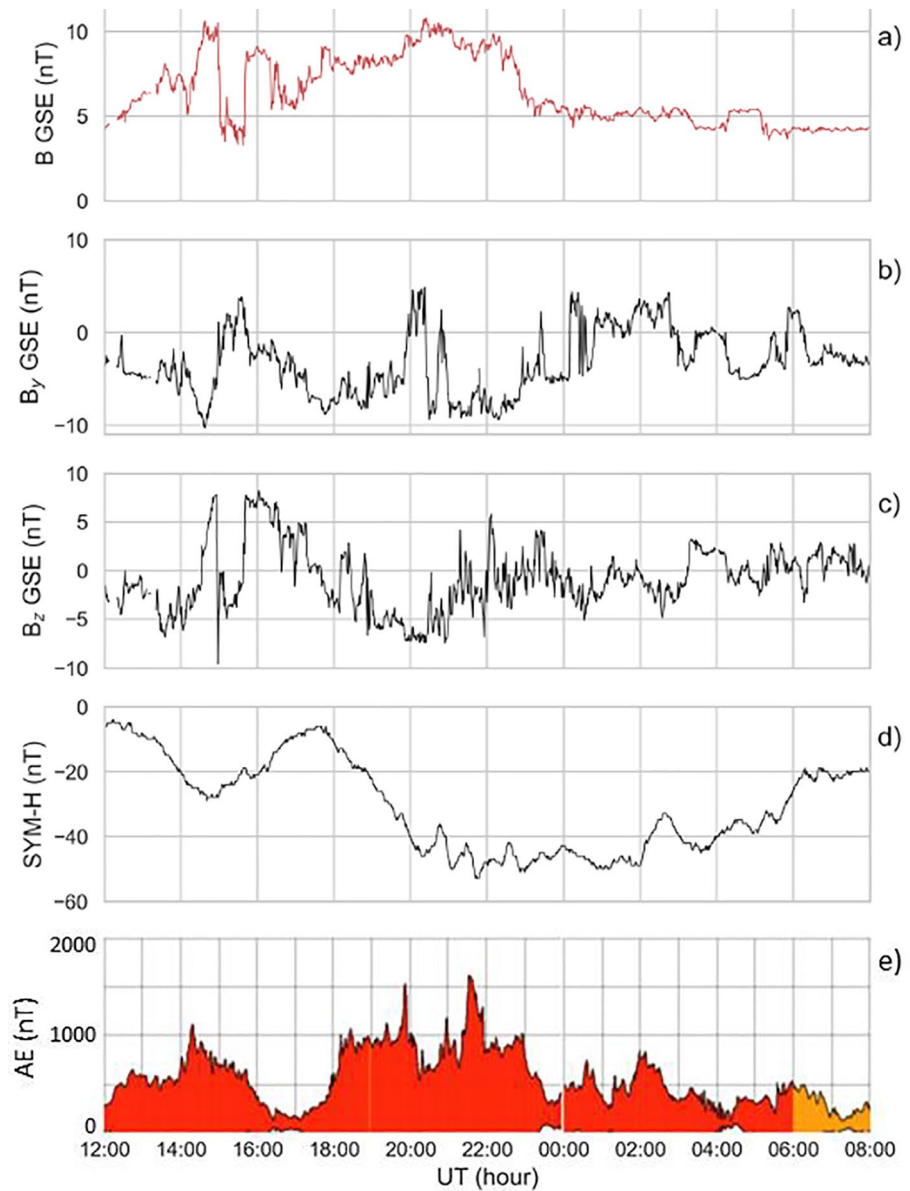
Figure 2. The interplanetary magnetic field (IMF) data time-shifted to the position of the bow shock, and the *AE* and *SYM-H* indices as a function of time, between 12:00 UT March 18th–08:00 UT March 19th: (a) the IMF B total magnitude, (b) IMF B_y component, (c) IMF B_z component, (d) *SYM-H* index, and (e) *AE* index.

07:00 UT. The rapid increases around 23:30 and 04:00 UT suggest the substorm activity and associated iono-spheric currents, as well as the expansion of the auroral oval. Furthermore, the *SYM-H* index (Figure 1d) is negative during the considered event, and a significant decrease in the *SYM-H* index is observed after 01 UT, with several pronounced minima at 02 UT (−20nT), 04:13 UT (−33nT), and 05:10 UT (−33nT).

3.2. Conditions for Case B: March 18–19th, 2018

The IMF conditions and geomagnetic indices *SYM-H* and *AE* during the second event on March 18–19th are shown in Figure 2. The strength of the IMF increases from ca. 5–10 nT between 12:00 and 15:00 UT. It generally stays between 7-10 nT until 22:40 UT, except for a rapid drop to 4 nT between 15:00 and 15:40 UT, while after 23:00 UT it returns to the usual values close to 5 nT (Prölss, 2004). The IMF orientation is highly variable.
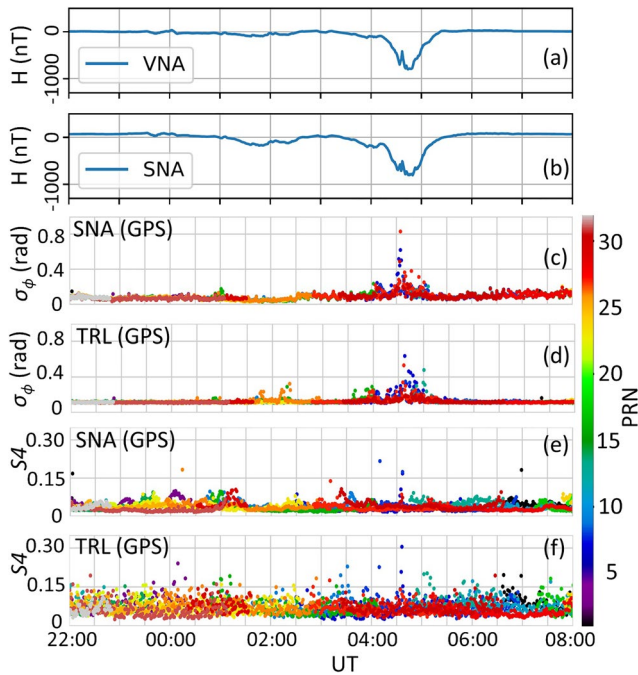
Figure 3. Variations in the *H* component of the Earth's magnetic field from the magnetometer stations in Neumayer (VNA) (a) and SANAE-IV (SNA) (b), phase scintillation (σ_φ) and amplitude scintillation (*S4*) indices from the SANAE-IV (SNA) (c) and (e) and Troll (TRL) (d) and (f) respectively as a function of time between 22:00 UT February 26th and 08:00 UT February 27th. The average magnetic field of each station is subtracted. The colors represent the PRN numbers corresponding to different GPS satellites.

The IMF B_y is mostly negative with some exceptions between 15:00-15:45 UT, 20:00-20:30 UT, and 00:00-03:00 UT (Figure 2b). Around 20:30 UT and 0 UT, the IMF B_y exhibits short-term excursions into positive values, while periods with longer values are observed afterward. Since the IMF B_y is negative during most of the event, the ionospheric footprint of the newly reconnected magnetic field lines on the dayside will be shifted in the SH toward morning hours and the convection cell on the evening side of the south polar cap should be larger for all configurations of the IMF B_z (Förster & Haaland, 2015; Heelis, 1984). Before 15:35 UT, the IMF B_z component is mostly negative with the strength of about −5 nT, except for a short period 14:30-15:00 UT coinciding with the increase in the IMF strength. B_z is positive between 15:45 and 17:38 UT, and then it remains largely negative until 21:15 UT (with values down to −7 nT). Afterward it is highly variable, switching between negative and positive values, but being mostly negative between 23:30 and 03:14 UT, thus facilitating magnetic reconnection on the dayside. The *SYM-H* index (Figure 2d) starts decreasing after 17:50 UT and reaches −47 nT at 20:20 UT. A slow recovery starts after 02:00 UT. Figure 2e shows the corresponding *AE* index, which reaches highest values between 14:20-16:00 UT (up to 1,000 nT) and 18:10-23:00 UT (with peaks up to 1,500 nT), suggesting increased geomagnetic activity during these periods of time.

4. Results

4.1. Case A: February 26–27th, 2018

Figures 3a and 3b show variations in the *H* component of the Earth's magnetic field at the Antarctic stations Neumayer (VNA) and SANAE-IV (SNA) respectively. There is no significant activity before midnight, and even after midnight, when the *AE* index shows significant activity (see again Figure 1), only moderate variations are seen in the magnetometer data. The *AE* index is based on the magnetometer stations in the NH, and if there are strong ionospheric currents in the SH around midnight, these will be far away from SANAE-IV and Neumayer. From midnight until 04:00 UT there are only small fluctuations, mainly at SNA between 01:15 and 02:30 UT. The major activity is observed after 04:00 UT, after the IMF B_z component was strongly negative for an extended period of time and when the *AE* index reaches high values. This corresponds to morning MLT hours at SANAE-IV and Neumayer: at both stations, a rapid decline in the magnetic field to about −800 nT starts at ca. 04:15 UT. The magnetic field recovers to previous values at ca. 05:30 UT.

The strong magnetic field variations correspond well to increased scintillations measured with the ground-based receivers. The values of phase (σ_φ) and amplitude (*S4*) scintillation indices at SANAE-IV and Troll stations are shown in Figures 3c–3f. Around 02:00 UT at Troll, we observe phase scintillations up to 0.4 rad, which might be linked to some localized ionospheric irregularities. There were no notable amplitude scintillations observed at neither of stations. The moderate variations in the magnetic field over SANAE-IV around 02 UT are not reflected in the scintillation indices over that station, but they coincide with increased levels of scintillation indices over Troll.

After 03:25 UT, the values of σ_φ increase over Troll, and after 04:00 UT they also increase over SANAE-IV. Significant phase scintillation indices at both SANAE-IV and Troll are observed at 04:30 UT with values reaching up to 0.9 rad. This corresponds to strong ionospheric currents that can be deduced from the magnetometer data. The amplitude scintillation index *S4* at SANAE-IV reaches values of 0.22 and 0.18 at 04:09 and 04:36 UT, and for Troll station up to 0.3 at 04:35 UT, although they are time-localized. This suggests that the signal paths, which were subject to scintillations passed through localized ionospheric plasma irregularities of the order of Fresnel's scale. Note that in Figure 3, the PRN numbers for the GNSS satellites are the same for SANAE-IV and for Troll stations both in the plot for σ_φ and for *S4*.
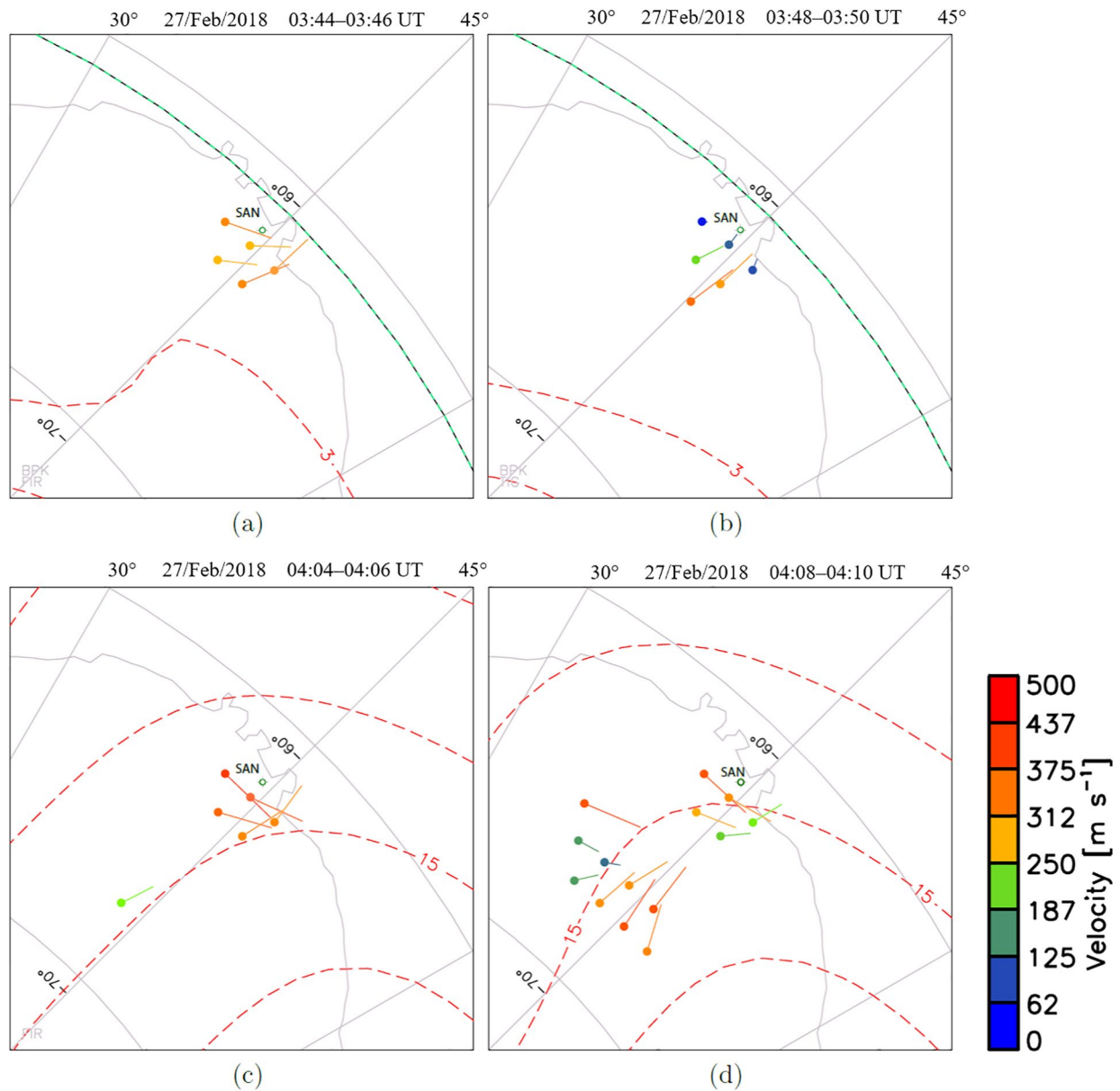
Figure 4. SuperDARN measurements from SANAE-IV at time intervals: 03:44–03:46 UT (a), 03:48–03:50 UT (b), 04:04–04:06 UT (c), 04:08–04:10 UT (d). The colors of the segments correspond to the speed of plasma. Dots denote positions of the measurements, while lines' direction and length correspond to the plasma velocity. The plots are presented in magnetic coordinates, and dashed lines correspond to equipotential lines deduced from the model fit.

We can note that for both stations the same satellites are subject to scintillations. At 05:30 UT phase scintillation index returns to quiet conditions, which coincides with the magnetic field H component returning to previous values.

SuperDARN can provide a large-scale view of plasma convection in the polar regions by feeding the radar measurements into a model. While there are only 7 radars observing the high latitude ionosphere in the SH, the radar at SANEA-IV is looking over Troll and these measurements can be directly used in our study. Figure 4 shows the SuperDARN measurements from SANAE-IV at four different time intervals between 03:44 and 04:10 UT, which correspond to the time period with moderate scintillations and just before the strong scintillations over SANAE-IV and Troll (SuperDARN data from SANAE-IV were not available after 04:10 UT). We observe that at 03:44 UT there is a northbound movement east of SANAE-IV, and eastbound movement west of SANAE-IV with plasma convection speeds between 250–375 m/s. Four minutes later, the
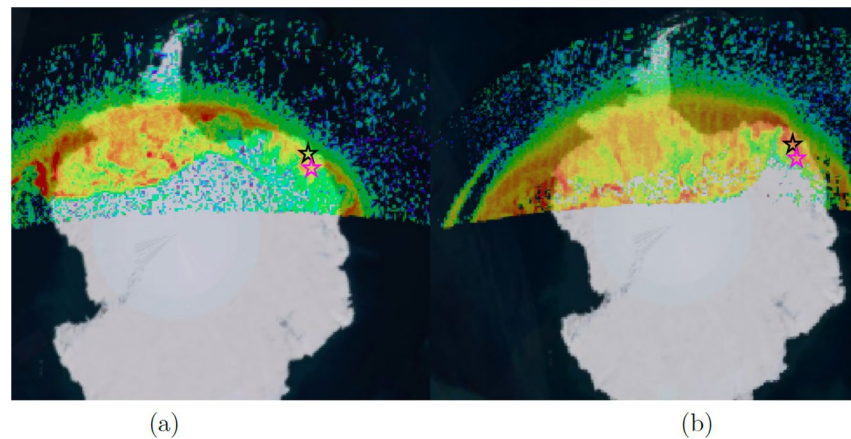
Figure 5. The intensity of the UV light in the LBH-L spectrum measured by the DMSP satellites passing over Queen Maud Land and West Antarctica: satellite F18 at 04:20 UT (a) and satellite F17 at 04:30 UT (b). The data is provided without the intensity scale. Stars indicate locations of receivers at SANAE-IV (black) and Troll (pink).

plasma movement is toward the north, with highly varying plasma speeds. At 04:04 UT east of the station, the directions are similar as in the first time interval, while the speeds have increased. Four minutes later, there is significantly more backscatter from plasma irregularities. Far south of the station, the movement is toward north and northeast, with speeds up to 500 m/s. Close to the station, and southwest from it, the plasma moves toward the east with speeds up to 375 m/s, while southeast from it, the direction is north and the speeds are slightly lower. Thus, one can expect that plasma irregularities over Troll and SANAE-IV should move from south to north, in a slightly easterly direction, which also agrees with the fitted equipotential lines (dashed lines).

To get a better insight into plasma structures over Queen Maud Land, we use data from the DMSP satellites. In Figure 5, the large-scale maps the UV light intensity due to auroral emissions obtained over a time period of 20 min with the SSI instrument are shown for the orbits of satellites F18 (Figure 5a) and F17 (Figure 5b) passing over Troll. It is clear that the auroral oval extends north over Troll during the pass of F18 and its edge moves further equatorward 10 min later during the pass of F17. The DMSP passes of F18 and F17 correspond to the increasing values, and are just before the peak values of σ_φ and $S4$ over Troll and SANAE-IV. The measurements of ion density and ion velocity by the DMSP satellites over Troll and SANAE-IV are shown in Figure 6. This DMSP data has a level-1 quality (with no quality flags to identify bad data). So this data should be used carefully. Therefore, we used only those measurements that were not in doubt. Erroneous ones have been deleted.

For DMSP F18 (Figure 6a) the ion density increases to 2×10^4 cm^{-3} before 04:19 UT and then drops to low values. It increases again to 2×10^4 cm^{-3} for a short time and then falls to 0.5×10^4 cm^{-3}. In the period 04:19–04:23 UT, there are large variations in speed. The ion density measured by DMSP F17 (Figure 6b) increases from 0.7×10^4 cm^{-3} up to 2.5×10^4 cm^{-3} at 04:30 UT. Then the plasma density fluctuates rapidly between 0.5×10^4 cm^{-3} and 2×10^4 cm^{-3} until 04:32:30 UT and stays at values around 0.5×10^4 cm^{-3}. The ion velocity shows low values before 04:30 UT, and large variations (up to 2 km/s) in the ion velocity are measured afterward. Thus, the satellite measurements confirm that there were both variations in the plasma density followed by strong variations in plasma velocity measured by the DMSP satellites (Liu et al., 2018). This suggests variations in the plasma density at the edges of the auroral oval and consequent strong flow shears within it (Spicher et al., 2020). In particular, DMSP 17 has measured highly structured plasma density at the edges of the auroral oval, followed by strong plasma flows.

To inspect spatial distributions of irregularities, we plot in Figure 7 the geographical locations of IPPs of the GPS satellites with the corresponding σ_φ values for a time period corresponding to the DMSP overpasses. This time period corresponds to the time when the magnetic field's H component gets strongly negative over SANAE-IV and Neumayer, and it is also after the last plot from SuperDARN at 04:10 UT, which showed plasma convection toward north-east with speeds up to 437 m/s (see again Figures 3 and 4d). We used
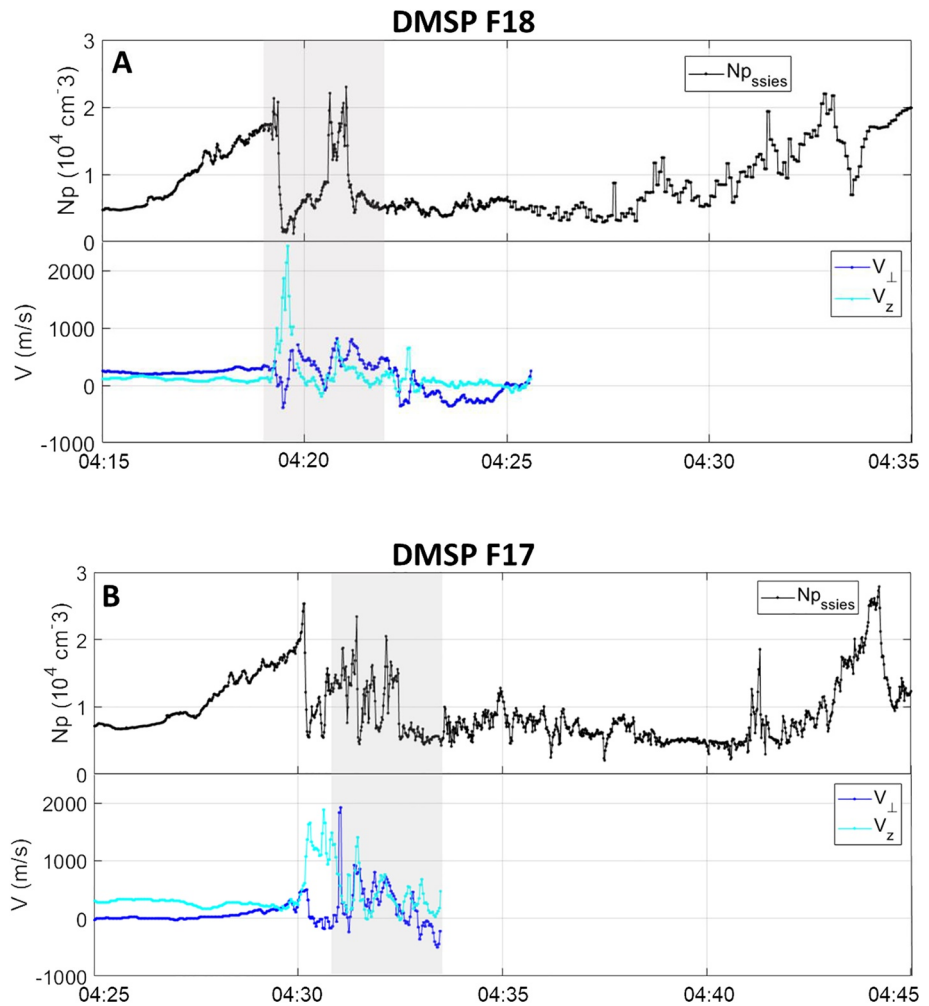
Figure 6. Data from DMSP F18 (a) for time interval 04:15–04:35 UT and from DMSP F17 (b) for time interval 04:25–04:45 UT. Top panels show the ion density, and bottom panels show the ion velocity in the perpendicular ($v_\perp$) and vertical (v_z) directions. The perpendicular direction is approximately parallel to the ground, while the vertical is positive away from the ground. The altitudes of the satellites are just under 880 km. Both satellites move in the southwest direction over Queen Maud Land. The shadowed area shows the moment in time when the satellites flew over the region of the receiver (see Figure 7).

corresponding maximum values for the color bars (Figures 7a and 7b). At 04:18 UT only weak scintillations (<0.2 rad) are observed from two satellites north of the two stations. One minute later, when DMSP F18 enters the field of view, σ_φ gets stronger for one of these GPS satellites and negligible for the other. At 04:20 UT DMSP F18 enters the region where noticeable σ_φ has already been observed for two minutes, and it measures significant variations in the plasma density and velocity around this time. Scintillations associated with the signal of other GPS satellites are still at low levels, and this suggests that at this particular time plasma structures related to scintillations are localized and might be related to a relatively stable auroral arc. Only after DMSP F18 leaves the field of view at 04:23 UT, more scintillations with values up to 0.19 rad appear over Troll and SANAE-IV.

Seven minutes later, in the time interval 04:30-04:36 UT, the DMSP F17 satellite passed over both stations (see Figure 7b, note that the scale of the color bar is different). This time period is related to the main phase of the substorm and expansion of the auroral oval (see again Figure 5b). At 04:30 UT, σ_φ reaches 0.35 rad on signal from the GPS satellite located north-west from the stations. While the DMSP F17 satellite moves from 68ºS, 8ºE to 70ºS, 4ºE, and it measures rapid fluctuations in the ion density, and velocities of ca. 1,000 m/s in perpendicular and vertical directions, there is an increase in the values of the phase scintillation index

over the area. In the interval 04:32–04:33 UT, we observe $\sigma_\varphi > 0.3$ rad on several GPS signals. During this time, the DMSP satellite is passing over Troll, and it first measures highly fluctuating ion density and velocity, and then after 04:32:30 a relatively stable ion density at 0.5×10^4 cm^{-3}. Intensified fluctuations in the signal phase, with $\sigma_\varphi > 0.45$ rad are observed with the SANAE-IV receiver on the westernmost satellites, while there are weaker phase scintillations toward the east. After 04:34 UT DMSP F17 enters a region with highly fluctuating ion velocities as it gets further into the expanding auroral oval. It is further south than the IPP of the GPS satellites, but at this time we observed σ_φ increase up to 0.85 rad. At 04:35 UT, there are only four satellites with good data (three of them have $\sigma_\varphi > 0.3$ rad), while the phase measurements for
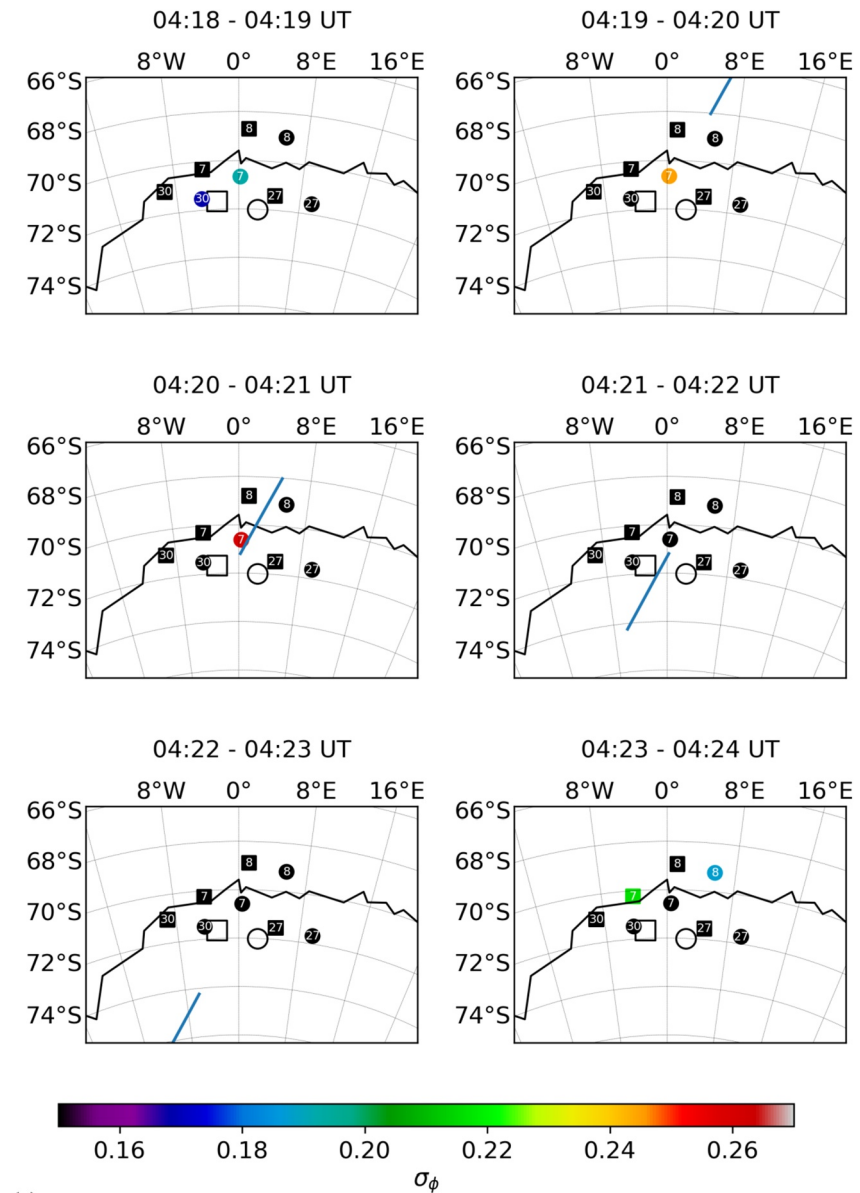
Figure 7. Positions of ionospheric piercing points for the GPS satellites in geographical coordinates. The color indicates the strength of σ_φ on the signal from the corresponding GPS satellites. The circles are the measurements from Troll and squares from SANAE-IV. The open square and circle are the positions of SANAE-IV and Troll, respectively. The blue line marks the orbit of the Defense Meteorological Satellite Program (DMSP) satellites traveling from northeast to south-west in a given time interval. Each panel corresponds to time intervals of 1 min between 04:18–04:24 UT for DMSP F18 (a) and 04:30–04:36 UT for DMSP F17 (b). Note that the color scale ranges are different in both panels. The digits in symbols represent the corresponding PRNs.
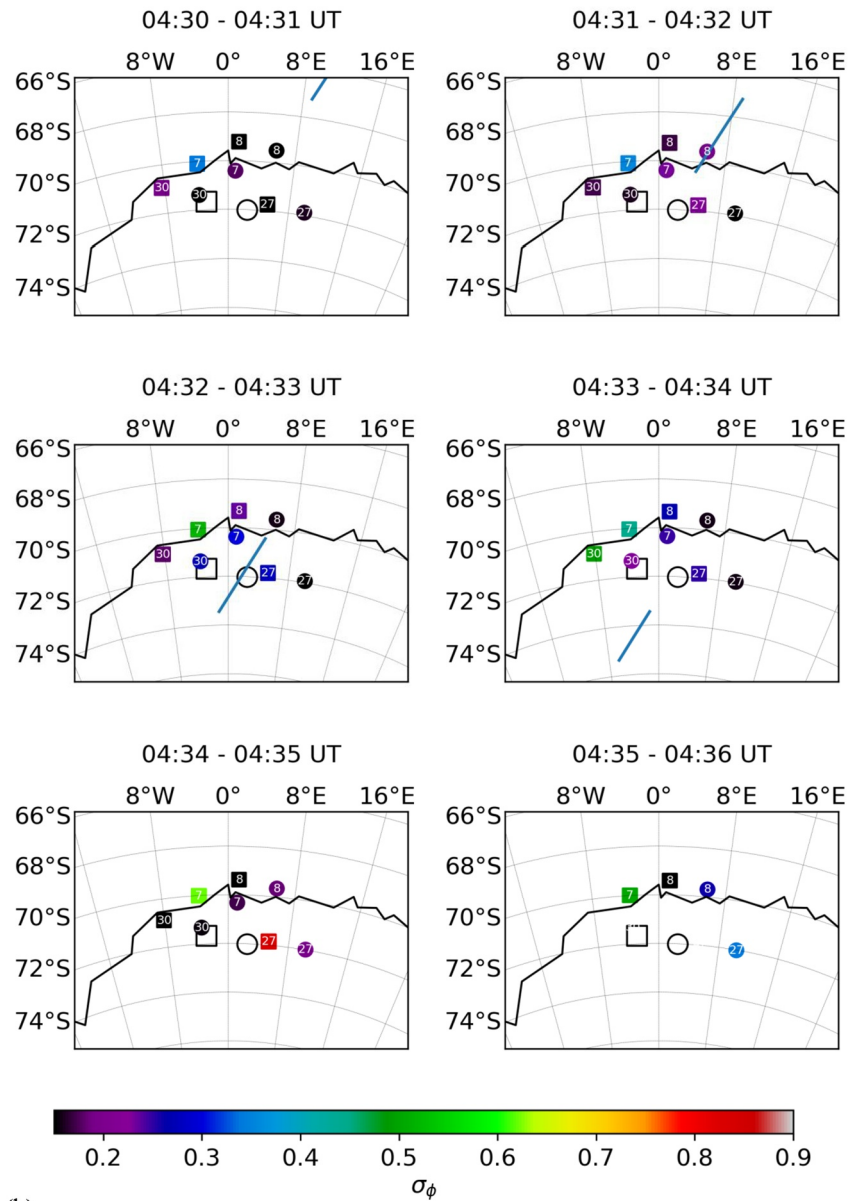
Figure 7. *Continued.*

other satellites gave extreme values of $\sigma_\varphi > 1$ rad. It is worth noting that for both receivers σ_φ for satellite PRN 30 reaches erroneously large values, and these data are not shown in the corresponding plot. Thus, the highest values of phase scintillation indices, and correspondingly largest variability of plasma over Troll and SANAE-IV are associated with the expanding auroral oval during a substorm event. They are also associated with structured plasma at the edges of the auroral oval and strong flow shears leading to plasma mixing during the expansion phase of the substorm. We note that although there might be some time-offset between the measurements, due to the geometry of the Earth's magnetic field and different altitudes of IPPs and DMSP satellites, a close inspection of Figures 5–7 confirms our findings on the expanding auroral oval and associated flow shears.
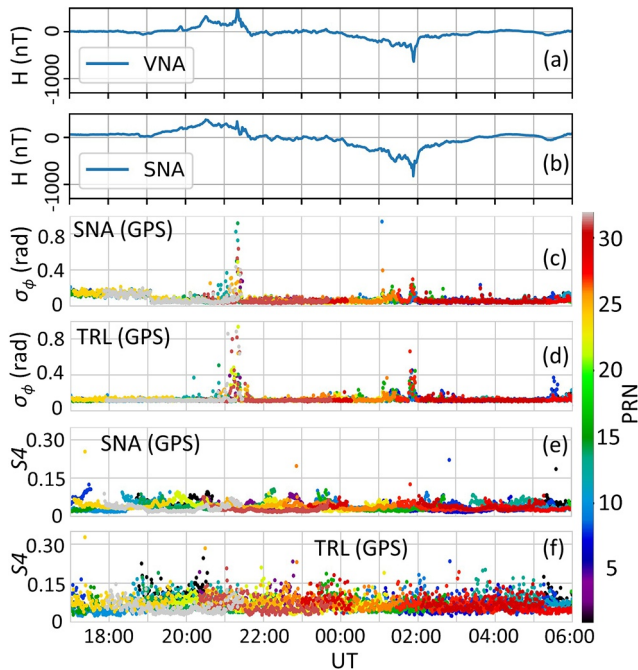
Figure 8. Same as in Figure 3 but for a time period between 17:00 UT March 18th–06:00 UT March 19th.

4.2. Case B: March 18–19th, 2018

On March 18–19th 2018, the IMF B_z was negative for several extended periods of time (see again Figure 2), and thus one can expect enhanced ionospheric convection and the substorm activity. The measured variations in the magnetic field's H component at Neumayer and SANAE-IV are shown in Figures 8a and 8b, respectively. There is a gradual increase in the H component of the magnetic field after 19:00 UT. At SANAE-IV it reaches a maximum around 20:30 UT with the value of ca. 300 nT and returns to normal value around 22:00 UT. A similar increase starting a bit later, at 19:50 UT is observed at Neumayer with a maximum of 450 nT at 21:23 UT. At 02:00 UT, the magnetometer data show a local minimum (−800 nT at SANAE-IV and −700 nT at Neumayer). The magnetic field measurements show little variations after 03:30 UT.

The corresponding scintillation indices from both receivers are shown in Figures 8c–8f. At 20:30 UT the amplitude scintillation index at Troll reaches 0.3 for selected satellites, but $S4$ observations at SANAE-IV do not show any clear peaks. Between 20:50-22:00 UT high phase scintillation indices up to 1 rad are recorded at both SANAE-IV and Troll indicating high structuring in the ionospheric plasma density. At the same time, $S4$ measurements from Troll show a small increase up to 0.2. We note that phase scintillations are observed at Troll earlier than at SANAE-IV.

There is another activity observed between 01:00 and 02:00 UT. Again, the two peaks in the phase scintillation indices were at Troll (up to 0.4 and 0.7 rad). While at Troll σ_φ are up to 0.7 rad, the corresponding data at SANAE-IV show smaller values up to 0.4 rad. Afterward, moderate values of phase scintillation indices are observed until 03:00 UT at both Troll and SANAE-IV, being more significant at Troll, and some smaller events are also observed at 05:30 UT at Troll. In the $S4$ measurements after midnight, we note one peak of about 0.22 for both stations for the same PRN number at 02:48 UT. Generally speaking, σ_φ variations correspond well to the positive (negative) variations in the magnetic field before (after) midnight.

To look closer into the dynamics of plasma irregularities over Queen Maud Land during this event, we show in Figure 9 the SuperDARN measurements over Troll and south of SANAE-IV for the time interval 20:54–21:20 UT. At 20:54 UT the irregularities move mostly toward the west at relatively low speeds following the well-established convection pattern. The station is located close to the edge of the convection cell, and some disturbances related to the flow shears can be expected and might lead to a locally perturbed flow pattern. Close to the edge of the cell, the flow velocity is lower, down to 125 m/s, while further south the velocities are about 375 m/s. At 20:58 UT closest to SANAE-IV the speed has increased to about 250 m/s at the edge and up to 875 m/s further south. This difference in velocities, with larger speeds in the south, is clear in all plots.

At 21:27 UT Troll's and SANAE-IV's magnetically conjugate points, which are located south-east of Greenland, were in the field of view of the DMSP F17 satellite. The satellite picture of the auroral activity in the UV light and a wide aurora is observed extending far south of Greenland (data not shown in figures). Assuming symmetric response in both hemispheres, one could expect similar large auroral activity in the SH. However, to confirm this, direct observations would be beneficial.

In Figure 10 we present the IPPs of the signal from the GPS satellites over Troll and SANAE-IV in geographical coordinates, and the highest levels of the corresponding phase scintillation indices σ_φ within each three-minute interval. Between 21:06 UT and 21:09 UT, we observe σ_φ with values about 0.25–0.45 rad for some satellites in the west and north of both stations. Between 21:09-21:15 UT, higher values of σ_φ are observed with the Troll receiver toward west and north, and σ_φ up to 0.35 rad for one satellite in the east observed from SANAE-IV. As there are more scintillations observed at Troll, it seems that irregularities are closer to this station. After 21:15 UT σ_φ reaches high values for satellites in all azimuthal directions from the stations, observed first at Troll, and then at SANAE-IV. This indicates that the irregularities are indeed
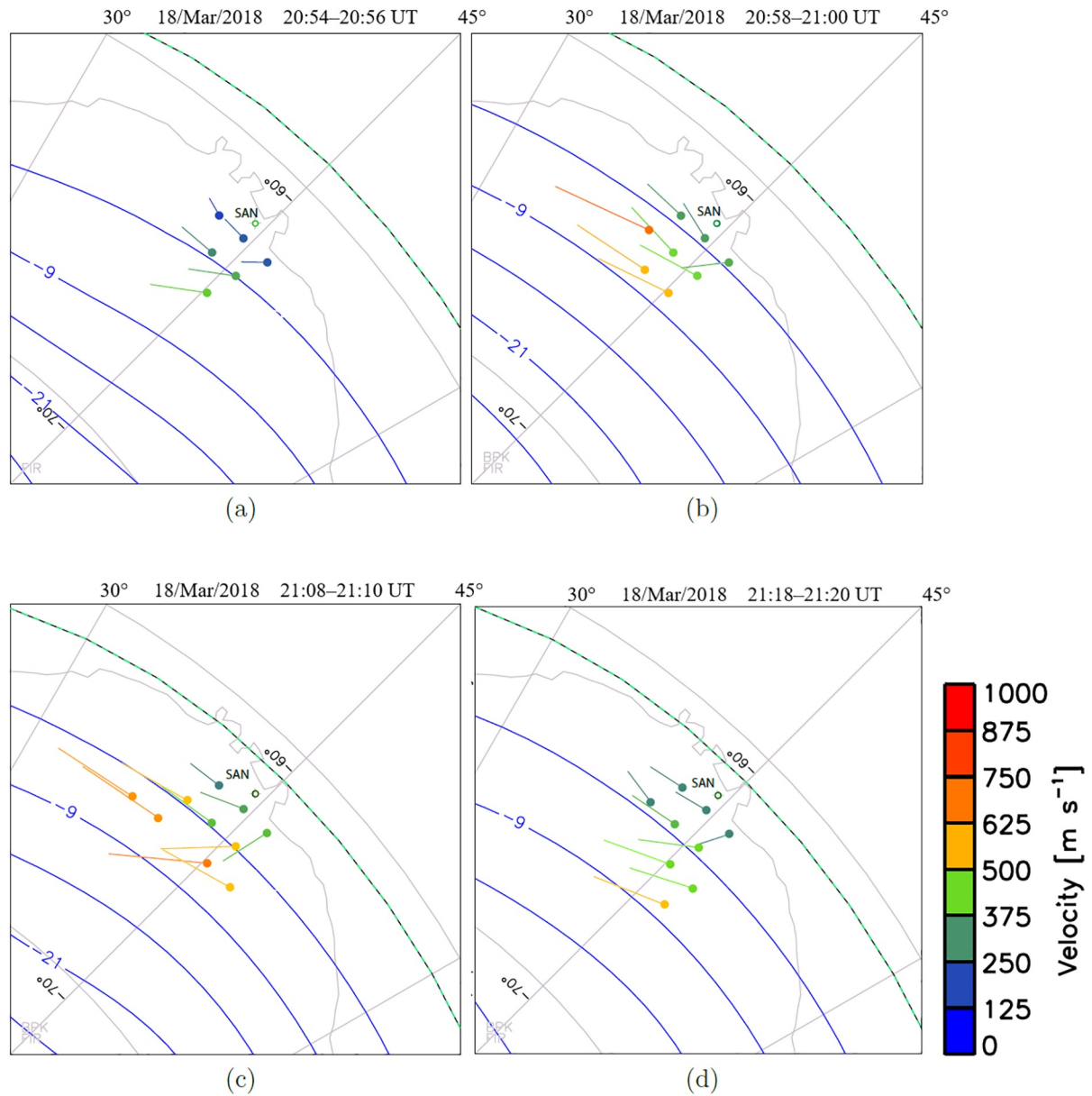
Figure 9. SuperDARN measurements from SANAE-IV for time intervals: 20:54-20:56 UT (a), 20:58-21:00 UT (b), 21:08-21:10 UT (c), 21:18-21:20 UT (d) on March 18. The colors of the segments correspond to the speed of plasma. Dots denote positions of the measurements, while lines' direction and length correspond to the plasma velocity. The plots are presented in magnetic coordinates, and dashed lines correspond to equipotential lines deduced from the model fit.

coming from the east and north-east in agreement with the convection pattern. At this period of time there are more satellite signals with high fluctuations in phase, $\sigma_\varphi > 1$ rad, and they are not shown in the figure. Most of them are observed with the receiver at Troll. However, a satellite with PRN 12 showed erroneous values on both receivers. This rapid increase in the scintillation level is just after the flow shear is observed in the SuperDARN data with a change in velocity direction observed above the Troll station, and indicating ionospheric plasma moving in the south-west direction. Data from Troll show higher phase scintillation indices in comparison with SANAE-IV. We note that after 21:24 UT the scintillation levels are reduced for both stations, and the SuperDARN data shows no backscatter from the area over Troll and south of SAN-AE-IV, which results in a contraction of the modeled convection cell (not shown in the figures).
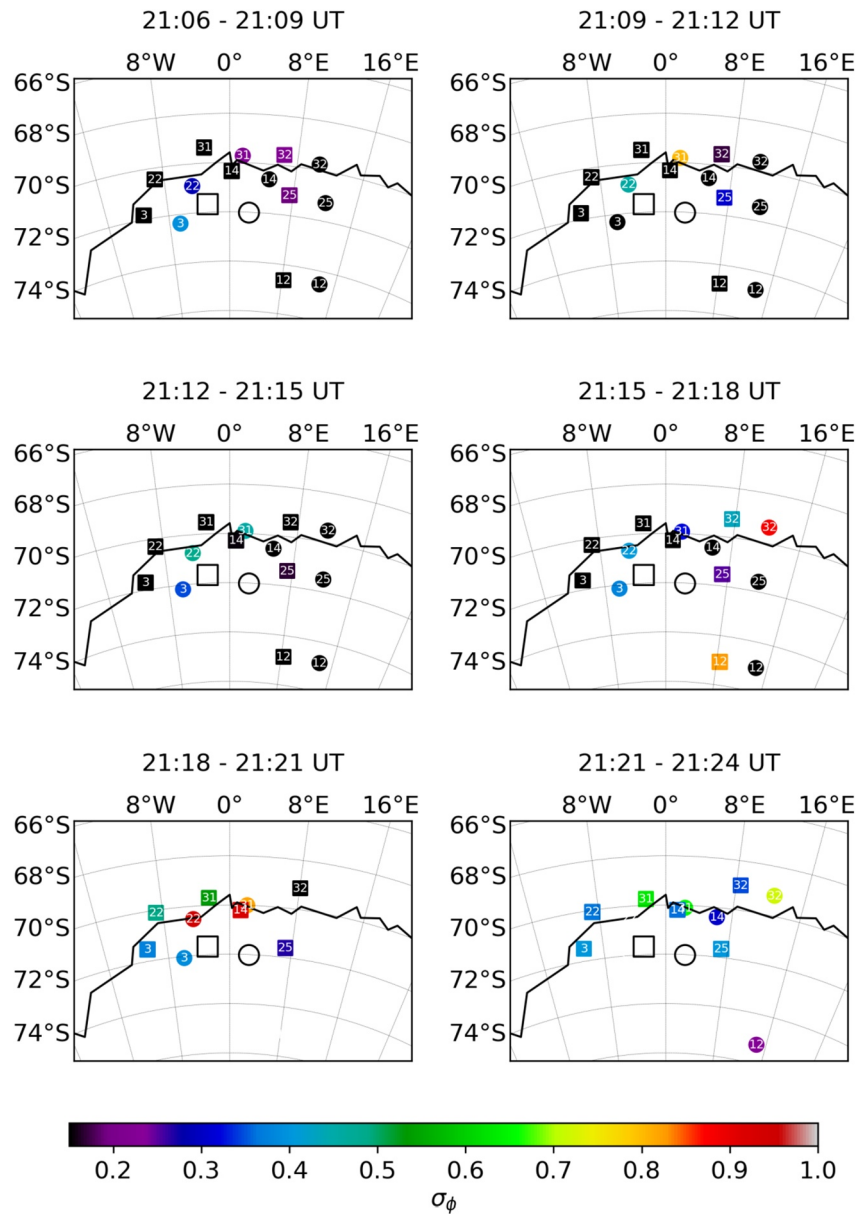
Figure 10. Positions of ionospheric piercing points for the GPS satellites in geographical coordinates. The color indicates the strength of σ_φ on the signal from the corresponding satellites. The circles are measurements from Troll and squares from SANAE-IV. The open square and circle are the positions of SANAE-IV and Troll respectively. Each panel corresponds to a given time interval of 3 min between 21:06–21:24 UT. The digits in symbols represent the corresponding PRNs.

5. Discussion

In this study, we used data from the recently installed GISTM receiver at the Norwegian Research Station Troll in Queen Maud Land, Antarctica, and data from complementary instruments at the nearby stations. We have identified two events in 2018 with high geomagnetic activity when all datasets were available: Case A: February 26–27th, and Case B: March 18–19th. For both cases, the solar wind data showed several periods of negative IMF B_z and B_y (except for events at 02:00 UT March 19 where B_y was predominantly positive and B_z slightly negative and close to 0 nT). Thus, the dayside reconnection was facilitated by the IMF orientation, and the ionospheric footprints of the reconnected magnetic field lines in the SH are shifted toward morning/noon hours (Förster & Haaland, 2015; Heelis, 1984; Reiff & Burch, 1985). In both cases,

the increased scintillation levels over Troll were observed in the evening and at night/morning hours. For Case A we identified a substorm which is observed also in the morning hours (see again Figure 3), while for Case B, there were two distinct geomagnetic activities recorded in Queen Maud Land (around 21:30 UT and 02:00 UT, see again Figure 8).

Combining data from different instruments allows us to get insight into physical processes leading to the formation of irregularities and observed increased levels of scintillation indices over Troll. We first take a closer look at the substorm in Case A. The substorm has a clear signature in the magnetometer data around 4:30 UT. The IMF B_z component was steadily negative since 03 UT, and hence it could facilitate reconnection on the dayside and lead to enhanced ionospheric convection. The *AE* index of about 1,000 nT indicated large ionospheric current in the auroral zone in the NH. From the magnetometer data we deduce that a strong westward ionospheric current was also present over western part of Queen Maud Land. Strong electrojets are shown to give scintillations, but usually stronger scintillations are associated with the poleward side of the electrojet (Jacobsen & Schafer, 2012; Prikryl et al., 2016), while Troll is on the equatorward side of the auroral oval. The spatiotemporal distribution of σ_φ over Troll and SANAE-IV show that plasma irregularities were traveling in the north-east direction in agreement with the plasma velocities entering the morning convection cell observed by the SuperDARN radar at SANAE-IV.

During the substorm event, we also observed a localized increase in the amplitude scintillation index *S4*, which suggests structuring of plasma down to the Fresnel scale of about 360 m and corresponding diffraction on the signal leading to amplitude scintillations. To test this, we also plotted the ionosphere-free linear combination (IFLC) to identify variations related to nonrefractive variations as it was done by McCaffrey and Jayachandran (2019). We present additional plots in the Supporting Information (Figures S2 and S3). Analyzing the behavior of detrended phase measurements together with IFLC at the Signal Type L1CA and L5Q and indications of the *S4* and σ_φ, one can indeed note the presence of variations in a very narrow time period about 04:37 UT that are related to nonrefractive processes in plasma. At this point in time, it is incorrect to calculate TEC, as well as the rate of change of TEC (ROT). However, these variations in *S4* are much lower and more localized than in σ_φ. Thus, in addition to the diffraction effects, there are strong refractive effects (to which the *S4* index is less sensitive, see McCaffrey and Jayachandran (2019)), which indicates the presence of larger scale irregularities. For calculating σ_φ, a standard procedure was used, and the raw phase measurements were detrended with a 6th-order Butterworth high-pass filter with a 0.1 Hz cutoff frequency. At high latitudes, where the ionospheric plasma drifts are between ~100 m/s and 1,500 m/s (e.g., MacDougall & Jayachandran, 2001), these measurements can be influenced by the effective changes in the Fresnel frequency due to plasma drift (Wang et al., 2018). In Case A, the SuperDARN radar at SANAE-IV measured the ionospheric drifts of about 375 m/s at 04:08 UT and 600 m/s at 04:35 UT. Hence, σ_φ is also including larger scale irregularities, and is reflecting the overall variability and structuring of plasma.

The DMSP F18 satellite passes over Queen Maud Land and West Antarctica during the initial phase of the substorm. It observes aurora (see again Figure 5a) and measures significant variations in the plasma density and moderate variations in velocity when passing over Troll. DMSP F17 passes during the main phase of the substorm and observes more intense aurora and the expanding auroral oval (Figure 5b). The decrease in plasma density when DMSP F17 enters the oval is followed by significant density gradients and variations in velocity. Thus, the flow shears in the expanding auroral oval lead to structuring of the equatorward edge of the oval. Moreover, energetic particle precipitation should also contribute to the plasma variability, especially after 04:34 UT, when DMSP F17 entered further into the oval, and encountered significant vertical velocity components. At the same time, higher σ_φ values indicate structures in ionospheric plasma during the pass of DMSP F17 (see again Figure 7b). This agrees with previous works, where it was shown that σ_φ were associated with structures due to gradient-drift instability, which are co-located with strong gradients in TEC at the edge of the plasma stream or of the auroral oval boundaries (see e.q., Mitchell et al., 2005; Moen et al., 2013; Spogli et al., 2009; Spicher et al., 2020). However, our results adhere to the findings by Jin et al. (2017), which show that the reason of largest structuring of plasma and hence highest σ_φ values, is a complex interplay of flow shears, density gradients and energetic particle precipitation, and the relevant instability mechanisms. While Jin et al. (2017) focused on the cusp region in their work, here we refer to the equatorward side of the expanding auroral oval. Consequently, in Case A, the most intense scintillations over Troll are associated with the expanding auroral oval during the main phase of a substorm, when the

auroral boundary is moving north of Troll, and the associated plasma structuring at the edges of the auroral oval (Prikryl et al., 2015), which is combined with the auroral particle precipitation and facilitated by significant flow shears leading to the mixing of plasma.

In Case B, the activity between 20 and 22 UT, which can be identified in the *AE* index (see again Figure 2), gives an increase in the magnetic field indicating eastward currents in the SH consistent with the convection electrojet in the evening convection cell. The magnetometer data from several stations in the NH (not shown in the figures) indicate that a substorm occurred at 21:30 UT which also corresponds to the peak in the *AE* index. The IMF B_y component is strongly negative before and during this event, and this can lead to enhanced ionospheric convection and auroral particle precipitation in the SH.

SuperDARN's measurements show high ionospheric plasma speeds (Figure 9), and rapid changes of velocities suggest the presence of plasma irregularities in the ionosphere and plasma mixing. These irregularities might be the result of structured plasma patches that have been convected over the polar cap and then entered the auroral oval on the night-side to form so-called blobs (blobs type 1, as defined in Jin et al. (2016)) which were then transported over Troll/SANAE-IV. There are few studies on how far such blobs can be transported, and Crowley et al. (2000) have shown that it is a possible scenario. In fact, the large scale convection cells deduced from the SuperDARN data (presented in the Figure S4) show fast convection of up to 1 km/s and highly structured plasma in the SH polar cap, which suggests that such a transport is likely. However, with a limited spatial coverage of ground-based instruments in the SH, it is difficult to confirm that indeed such a structured blob was the cause of scintillations.

SuperDARN shows high plasma velocities far south of SANAE-IV, and the plasma over Troll and SANAE-IV comes predominantly from the east, following the convection pattern. During this period, there are significant differences in speed at short distances, which can lead to the Kelvin-Helmholtz instability and corresponding irregularities (Keskinen et al., 1988). SuperDARN model estimates that SANAE-IV is at the edge of the convection cell. In the area around the Troll's conjugate point, the DMSP satellite observed aurora activity extending far south of Greenland (around 20 MLT). In Case B, around 21:20 UT there were high values of σ_φ observed over Troll. As in Case A, we plotted the IFLC for different satellites at this time (see Figure S3). All considered satellites show variations in IFLC, which also indicate nonrefractive nature of phase fluctuations. At the same time, we do not observe significant increase in *S4* values, which usually is an indication that there are no diffraction effects. However, the absence of amplitude scintillations (when *S4* is low) and the presence of high phase scintillations was discussed in the work by Ghobadi et al. (2020). They indicated the presence of small-scale irregularities in the ionosphere, which did not result in significant *S4* values. Therefore, phase variations, which we observed in Case B, can be both refractive (due to larger scale irregularities) and nonrefractive (due to small-scale irregularities). These irregularities are associated with the flow shear instabilities and can also be modulated by the auroral particle precipitation (Spicher et al., 2020).

The second geomagnetic event at around 02 UT (corresponding to local midnight) gives a decrease in the magnetic field, indicating westward auroral electrojet. The *AE* index shows an increase of about 850 nT. When the H-component dips to its minimum value, we can assume auroral activity in this area. For positive IMF B_y and slightly negative B_z, the tilt in the two-cell convection pattern vanishes and the cross-polar flow should be almost aligned with the noon-midnight meridian (Förster & Haaland, 2015). Our stations are just under the zone of this main flow channel. Changes in magnetic field are correlated well with changes in σ_φ. Observations of the amplitude scintillations *S4* at 01:45 and 02:48 UT, together with changes in σ_φ, suggest that the diffraction effect is caused by irregularities of the order of 300–400 m. There are more fluctuations in the signal phase than in amplitudes of the transionospheric radio signals. Thus, σ_φ also includes the refractive effects due to large-scale irregularities. Strong plasma flows modulated by the auroral particle precipitation on the nightside of the oval can be the source of these irregularities.

Several factors need to be taken into account when analyzing the results. The receiver types in SANAE-IV and Troll are different, the cutoff frequency used for calculations of σ_ϕ index was 0.1 Hz, which can affect the values of scintillation indices to some degree. For the two considered Cases A and B, both receivers showed erroneous σ_φ values on the satellite with the same PRN. We looked at the possible causes of these errors, but neither the low C/N0 or Lock time less than 240 s was the cause. Using the BESTPOS data, we also

calculated, with a resolution of 10 s: STD latitude, longitude and altitude of the Troll receiver. However, we do not see that there is a strong impact on the positioning, seemingly because the irregularities were localized and affected selected satellites. We used the altitude of 350 km as the commonly used height for a thin ionospheric layer to calculate IPP's, but the actual altitude of irregular layers might be lower. Therefore, we also checked the IPPs with altitudes at 120 km in the E layer of the ionosphere, as it was suggested by Prikryl et al. (2013). The comparison of these results with direct measurements by DMSP F17 and F18 gives better agreement for IPPs at 350 km of altitude. Note again that a potential offset in time of these measurements due to geometry of the Earth's magnetic field does not impact our general findings. For the exact altitude of IPP it would be advisable to use observations with an ionosonde and the coherent scattering radars, however no such data are currently available. Many conclusions on physical processes in Antarctica are based on the SuperDARN data. The SuperDARN model is a statistical model based on the measurements and meant to characterize periods of stable IMF. In the SH there are fewer data points, therefore the convection is not regular and errors are possible especially during auroral substorms (Fiori et al., 2010). In this case, it is good to support the model calculations with the satellite data and all-sky cameras, however, the satellite conjunctions for the ground-based measurements are relatively rare.

6. Conclusions

We have presented the first results based on data from the GISTM receiver at the Norwegian Research station Troll in Queen Maud Land, Antarctica. To complement this data set, we used data from the GISTM receiver and SuperDARN radar at SANAE-IV research station, located 186 km from Troll, and other complementary datasets, such as magnetometer data from SANAE-IV and Neumayer stations, and data from the DMSP satellites.

Our case studies show that using multiple instruments can provide insight into the causes and scales of ionospheric plasma irregularities and thereby their influence on the GNSS signals. DMSP and SuperDARN data indicate that irregularities over Troll are associated with the expanding auroral oval during a substorm event and that they are related to plasma structuring at the equatorward edge of the auroral oval due to strong flow shears leading to plasma mixing during the expansion phase. They form fast moving large-scale plasma irregularities, which can lead to predominantly refractive variations in the phase of the signal. SuperDARN data suggests that it might have been possible to transport a structured plasma blob over to Troll/SANAE-IV. Significant variations in the plasma flow velocity at short distances over Troll are likely to result in the flow-shear instabilities, which can lead to further plasma mixing.

Satellites data allow for studying the relationship between changes in the distribution of electron density and the occurrence of scintillations. In this study, we have used data from DMSP F17 and F18 satellites. A further combined approach can be done with the recently installed all-sky imager at Troll and the satellite data during conjunctions to study the relationship between scintillations on the GNSS signal and particle precipitation. The latter can also provide precise information whether the scintillations are due to structures at the edges or within the auroral oval.

Combining data from two closely located receivers in Antarctica allows tracking the spatiotemporal dynamics of ionospheric plasma irregularities (Kriegel et al., 2017). Ionospheric observations at Troll and SANAE-IV are important for increasing our understanding of the polar ionosphere in the southern hemisphere and give more insight into space weather effects in the southern hemisphere. Expanding the network of GISTM receivers in Antarctica would further facilitate this goal and provide better resolution of the measurements. Due to asymmetry in the Earth's magnetic field, the variability in the plasma will be different in both hemispheres. Case studies combined with statistical and climatological research will provide better insight into the differences between both hemispheres and hence a better understanding of the ionosphere as a whole.

Data Availability Statement

The DMSP data are available at NOAA's National Geophysical Data Center (https://www.ngdc.noaa.gov) and the SuperDARN data provided by Virginia Tech (http://vt.superdarn.org/tiki-index.php). Data from Troll station necessary to reproduce the reported findings are available at https://doi.org/10.5281/zenodo.3974293.

References

Alfonsi, L., Spogli, L., De Franceschi, G., Romano, V., Aquino, M., Dodson, A., & Mitchell, C. N. (2011). Bipolar climatology of GPS ionospheric scintillation at solar minimum. *Radio Science*, *46*(3), RS0D05. https://doi.org/10.1029/2010RS004571

Beach, T. L. (2006). Perils of the GPS phase scintillation index (σ_ϕ). *Radio Science*, *41*, RS5S31. https://doi.org/10.1029/2005RS003356

Chen, P., Li, Q., Yao, Y., & Yao, W. (2019). Study on the plasmaspheric Weddell Sea Anomaly based on COSMIC onboard GPS measurements. *Journal of Atmospheric and Solar-Terrestrial Physics*, *192*, 104923. https://doi.org/10.1016/j.jastp.2018.09.012

Cilliers, P. J., Alfonsi, L., Spogli, L., De Franceschi, G., Romano, V., Hunstad, I., et al. (2017). Analysis of the ionospheric scintillations during 20-21 January 2016 from SANAE by means of the DemoGRAPE scintillation receivers. In *2017 XXXIInd General Assembly and Scientific Symposium of the International Union of Radio Science. URSI GASS*. https://doi.org/10.23919/URSIGASS.2017.8105114

Clauer, C. R., Banks, P. M., Smith, A. Q., Jorgensen, T. S., Friis-Christensen, E., Vennerstrom, S., et al. (1984). Observation of interplanetary magnetic field and of ionospheric plasma convection in the vicinity of the dayside polar cleft. *Geophysical Research Letters*, *11*(9), 891–894. https://doi.org/10.1029/GL011i009p00891

Crowley, G., Ridley, A. J., Deist, D., Wing, S., Knipp, D. J., Emery, B. A., et al. (2000). Transformation of high-latitude ionospheric F region patches into blobs during the March 21, 1990, storm. *Journal of Geophysical Research*, *105*(A3), 5215–5230. https://doi.org/10.1029/1999JA900357

De Franceschi, G., Alfonsi, L., Romano, V., Aquino, M., Dodson, A. H., Mitchell, C. N., et al. (2008). Dynamics of high-latitude patches and associated small-scale irregularities during the October and November 2003 storms. *Journal of Atmospheric and Solar-Terrestrial Physics*, *70*(6), 879–888. https://doi.org/10.1016/j.jastp.2007.05.018

Deshpande, K. B., Bust, G. S., Clauer, C. R., Kim, H., Macon, J. E., Humphreys, T. E., et al. (2012). Initial GPS scintillation results from CASES receiver at South Pole, Antarctica. *Radio Science*, *47*, RS5009. https://doi.org/10.1029/2012RS005061

Fiori, R. A. D., Boteler, D. H., Koustov, A. V., Haines, G. V., & Ruohoniemi, J. M. (2010). Spherical cap harmonic analysis of Super Dual Auroral Radar Network (SuperDARN) observations for generating maps of ionospheric convection. *Journal of Geophysical Research*, *115*, A07307. https://doi.org/10.1029/2009JA015055

Förster, M., & Haaland, S. (2015). Interhemispheric differences in ionospheric convection: Cluster EDI observations revisited. *Journal of Geophysical Research: Space Physics*, *120*, 5805–5823. https://doi.org/10.1002/2014JA020774

Forte, B., & Radicella, S. M. (2002). Problems in data treatment for ionospheric scintillation measurements. *Radio Science*, *37*(6). https://doi.org/10.1029/2001RS002508

Ghobadi, H., Spogli, L., Alfonsi, L., Cesaroni, C., Cicone, A., Linty, N., et al. (2020). Disentangling ionospheric refraction and diffraction effects in GNSS raw phase through fast iterative filtering technique. *GPS Solutions*, *24*, 85. https://doi.org/10.1007/s10291-020-01001-1

Greenwald, R. A., Baker, K. B., Dudeney, J. R., Pinnock, M., Jones, T. B., Thomaset, E. C., et al. (1995). DARN/SuperDARN. *Space Science Reviews*, *71*, 761–796. https://doi.org/10.1007/BF00751350

Heelis, R. A. (1984). The effects of interplanetary magnetic field orientation on dayside high-latitude ionospheric convection. *Journal of Geophysical Research*, *89*(A5), 2873–2880. https://doi.org/10.1029/JA089iA05p02873

Horvath, I., & Lovell, B. C. (2009). Investigating the relationships among the South Atlantic Magnetic Anomaly, southern nighttime midlatitude trough, and nighttime Weddell Sea Anomaly during southern summer. *Journal of Geophysical Research*, *114*, A02306. https://doi.org/10.1029/2008JA013719

Jacobsen, K. S., & Schafer, S. (2012). Observed effects of a geomagnetic storm on an RTK positioning network at high latitudes. *Journal of Space Weather and Space Climate*, *2*, A13. https://doi.org/10.1051/swsc/2012013

Jin, Y., Moen, J. I., & Miloch, W. J. (2015). On the collocation of the cusp aurora and the GPS phase scintillation: A statistical study. *Journal of Geophysical Research: Space Physics*, *120*, 9176–9191. https://doi.org/10.1002/2015JA021449

Jin, Y., Moen, J. I., Miloch, W. J., Clausen, L. B. N., & Oksavik, K. (2016). Statistical study of the GNSS phase scintillation associated with two types of auroral blobs. *Journal of Geophysical Research: Space Physics*, *121*, 4679–4697. https://doi.org/10.1002/2016JA022613

Jin, Y., Moen, J. I., Oksavik, K., Spicher, A., Clausen, L. B. N., & Miloch, W. J. (2017). GPS scintillations associated with cusp dynamics and polar cap patches. *Journal of Space Weather and Space Climate*, *7*, A23. https://doi.org/10.1051/swsc/2017022

Kamide, Y., & Baumjohann, W. (1993). *Magnetosphere-Ionosphere Coupling*. Springer-Verlag Berlin Heidelberg. https://doi.org/10.1007/978-3-642-50062-6

Karpachev, A. T., Gasilov, N. A., & Karpachev, O. A. (2011). Morphology and causes of the Weddell Sea anomaly. *Geomagnetism and Aeronomy*, *51*, 812–824. https://doi.org/10.1134/S0016793211050070

Keskinen, M. J., Mitchell, H. G., Fedder, J. A., Satyanarayana, P., Zalesak, S. T., & Huba, J. D. (1988). Nonlinear evolution of the Kelvin-Helmholtz instability in the high-latitude ionosphere. *Journal of Geophysical Research*, *93*(A1), 137–152. https://doi.org/10.1029/JA093iA01p00137

Kim, H., Clauer, C. R., Deshpande, K., Lessard, M. R., Weatherwax, A. T., Bust, G. S., et al. (2014). Ionospheric irregularities during a substorm event: Observations of ULF pulsations and GPS scintillations. *Journal of Atmospheric and Solar-Terrestrial Physics*, *114*, 1–8. https://doi.org/10.1016/j.jastp.2014.03.006

Kinrade, J., Mitchell, C. N., Yin, P., Smith, N., Jarvis, M. J., Maxfield, D. J., et al. (2012). Ionospheric scintillation over Antarctica during the storm of 5–6 April 2010. *Journal of Geophysical Research*, *117*(A5), A05304. https://doi.org/10.1029/2011JA017073

Knight, H. K., Strickland, D. J., Hecht, J. H., Straus, P. R., Morrison, D., Paxton, L. J., & Evans, D. S. (2008). Evidence for significantly greater N2 Lyman-Birge-Hopfield emission efficiencies in proton versus electron aurora based on analysis of coincident DMSP SSUSI and SSJ/5 data. *Journal of Geophysical Research*, *113*, A04305. https://doi.org/10.1029/2007JA012728

Kriegel, M., Jakowski, N., Berdermann, J., Sato, H., & Mersha, M. W. (2017). Scintillation measurements at Bahir Dar during the high solar activity phase of solar cycle 24. *Annales Geophysicae*, *35*, 97–106. https://doi.org/10.5194/angeo-35-97-2017

Laundal, K. M., Cnossen, I., Milan, S. E., Haaland, S. E., Coxon, J., Pedatella, N. M.., et al. (2017). North-south asymmetries in Earth's magnetic field. *Space Science Reviews*, *206*(1–4), 225–257. https://doi.org/10.1007/s11214-016-0273-0

Li, G., Ning, B., Ren, Z., & Hu, L. (2010). Statistics of GPS ionospheric scintillation and irregularities over polar regions at solar minimum. *GPS Solutions*, *14*, 331–341. https://doi.org/10.1007/s10291-009-0156-x

Li, M., Yuan, Y., Zhang, B., Wang, N., Li, Z., Liu, X., & Zhang, X. (2018). Determination of the optimized single-layer ionospheric height for electron content measurements over China. *Journal of Geodesy*, *92*, 169–183. https://doi.org/10.1007/s00190-017-1054-6

Liu, M., Zhang, X. -X., He, F., & Wang, W. (2018). A long-term data set of vertical ion drift velocity at high latitudes constructed from DMSP measurements. *Journal of Geophysical Research: Space Physics*, *123*, 6090–6102. https://doi.org/10.1029/2018JA025504

MacDougall, J. W., & Jayachandran, P. T. (2001). Polar cap convection relationships with solar wind. *Radio Science*, *36*(6), 1869–1880. https://doi.org/10.1029/2001RS001007

McCaffrey, A. M., & Jayachandran, P. T. (2019). Determination of the refractive contribution to GPS phase "scintillation". *Journal of Geophysical Research: Space Physics*, *124*, 1454–1469. https://doi.org/10.1029/2018JA025759

Mitchell, C. N., Alfonsi, L., De Franceschi, G., Lester, M., Romano, V., & Wernik, A. W. (2005). GPS TEC and scintillation measurements from the polar ionosphere during the October 2003 storm. *Geophysical Research Letters*, *32*, L12S03. https://doi.org/10.1029/2004GL021644

Moen, J., Oksavik, K., Alfonsi, L., Daabakk, Y., Romano, V., & Spogli, L. (2013). Space weather challenges of the polar cap ionosphere. *Journal of Space Weather and Space*, *3*, A02. https://doi.org/10.1051/swsc/2013025

Ngwira, C. M., McKinnell, L. A., & Cilliers, P. J. (2010). GPS phase scintillation observed over a high-latitude Antarctic station during solar minimum. *Journal of Atmospheric and Solar-Terrestrial Physics*, *72*(9), 718–725. https://doi.org/10.1016/j.jastp.2010.03.014

Prikryl, P., Ghoddousi-Fard, R., Weygand, J. M., Viljanen, A., Connors, M., Danskin, D. W., et al. (2016). GPS phase scintillation at high latitudes during the geomagnetic storm of 17–18 March 2015. *Journal of Geophysical Research: Space Physics*, *121*, 10448–10465. https://doi.org/10.1002/2016JA023171

Prikryl, P., Jayachandran, P. T., Chadwick, R., & Kelly, T. D. (2015). Climatology of GPS phase scintillation at northern high latitudes for the period from 2008 to 2013. *Annales Geophysicae*, *33*(5), 531–545. https://doi.org/10.5194/angeo-33-531-2015

Prikryl, P., Jayachandran, P. T., Mushini, S. C., Pokhotelov, D., MacDougall, J. W., Donovan, E., et al. (2010). GPS TEC, scintillation and cycle slips observed at high latitudes during solar minimum. *Annales Geophysicae*, *28*(6), 1307–1316. https://doi.org/10.5194/angeo-28-1307-2010

Prikryl, P., Spogli, L., Jayachandran, P. T., Kinrade, J., Mitchell, C. N., Ning, B., et al. (2011). Interhemispheric comparison of GPS phase scintillation at high latitudes during the magnetic-cloud-induced geomagnetic storm of 5–7 April 2010. *Annales Geophysicae*, *29*(12), 2287–2304. https://doi.org/10.5194/angeo-29-2287-2011

Prikryl, P., Zhang, Y., Ebihara, Y., Ghoddousi-Fard, R., Jayachandran, P. T., Kinrade, J., et al. (2013). An interhemispheric comparison of GPS phase scintillation with auroral emission observed at the South Pole and from the DMSP satellite. *Annals of Geophysics*, *56*(2), R0216. https://doi.org/10.4401/ag-6227

Priyadarshi, S., Zhang, Q., & Ma, Y. (2018). Antarctica SED/TOI associated ionospheric scintillation during 27 February 2014 geomagnetic storm. *Astrophysics and Space Science*, *363*, 262. https://doi.org/10.1007/s10509-018-3484-x

Prölss, G. W. (2004). Introduction. In *Physics of the Earth's space environment* (pp. 1–9). Berlin, Heidelberg: Springer. https://doi.org/10.1007/978-3-642-97123-5

Reiff, P. H., & Burch, J. L. (1985). IMF By-dependent plasma flow and Birkeland currents in the dayside magnetosphere: 2. A global model for northward and southward IMF. *Journal of Geophysical Research*, *90*(A2), 1595–1609. https://doi.org/10.1029/JA090iA02p01595

Rino, C. L. (1979). A power law phase screen model for ionospheric scintillation: 1. Weak scatter. *Radio Science*, *14*(6), 1135–1145. https://doi.org/10.1029/RS014i006p01135

Shepherd, S. G. (2014). Altitude-adjusted corrected geomagnetic coordinates: Definition and functional approximations. *Journal of Geophysical Research: Space Physics*, *119*, 7501–7521. https://doi.org/10.1002/2014JA020264

Spicher, A., Deshpande, K., Jin, Y., Oksavik, K., Zettergren, M. D., Clausen, L. B. N., et al. (2020). On the production of ionospheric irregularities via Kelvin-Helmholtz instability associated with cusp flow channels. *Journal of Geophysical Research: Space Physics*, *125*, e2019JA027734. https://doi.org/10.1029/2019JA027734

Spogli, L., Alfonsi, L., De Franceschi, G., Romano, V., Aquino, M. H. O., & Dodson, A. (2009). Climatology of GPS ionospheric scintillations over high and mid-latitude European regions. *Annals of Geophysics-Germany*, *27*(9), 3429–3437. https://doi.org/10.5194/angeo-27-3429-2009

Wang, Y., Zhang, Q.-H., Jayachandran, P. T., Moen, J., Xing, Z.-Y., Chadwick, R., et al. (2018). Experimental evidence on the dependence of the standard GPS phase scintillation index on the ionospheric plasma drift around noon sector of the polar ionosphere. *Journal of Geophysical Research: Space Physics*, *123*, 2370–2378. https://doi.org/10.1002/2017JA024805

Workayehu, A. B., Vanhamäki, H., & Aikio, A. T. (2019). Field-aligned and horizontal currents in the Northern and Southern Hemispheres from the Swarm satellite. *Journal of Geophysical Research: Space Physics*, *124*, 7231–7246. https://doi.org/10.1029/2019JA026835

Yeh, K. C., & Liu, C. H. (1982). Radio wave scintillations in the ionosphere. *Proceedings of the IEEE*, *70*(4), 324–360. https://doi.org/10.1109/PROC.1982.12313

Reference From the Supporting Information

Carrano, C. S., Groves, K. M., McNeil, W. J., & Doherty, P. H. (2013). Direct Measurement of the Residual in the Ionosphere-Free Linear Combination during Scintillation. In *Proceedings of the 2013 International Technical Meeting of The Institute of Navigation* (pp. 585–596), San Diego, California.